AIAA JOURNAL
Vol. 47, No. 9, September 2009

Fluidic Control of Separation Over a Hemispherical Turret

Bojan Vukasinovic,* Daniel Brzozowski,† and Ari Glezer‡
Georgia Institute of Technology, Atlanta, Georgia 30332-0405

DOI: 10.2514/1.41920

Active control of flow separation over a hemispherical turret, that is, a surface-mounted hemispherical shell, is demonstrated in wind-tunnel experiments at Reynolds numbers up to 706,000. Control is applied using high-frequency ($St_D > 10$) actuation effected by a meridional array of individually addressable synthetic jet actuators. The control effectiveness is assessed and characterized using high-resolution particle image velocimetry, hot-wire anemometry, and surface pressure distributions. Measurements of the baseline flow indicate that separation occurs in a horseshoe pattern across the hemisphere with the apex at the plane of symmetry. High-frequency actuation results in a substantial reduction in the extent of the recirculating flow domain downstream of the turret by delaying separation, decreasing the reattachment length, and concomitantly suppressing the energy of the fluctuating motions. As a consequence, the core of the recirculating vortex is displaced toward the juncture between the hemisphere and the surface and its cross-sectional area is substantially diminished. Furthermore, the estimated turbulent kinetic energy in the controlled flow is decreased significantly, especially at the large scales. Deliberate tripping of the flow just upstream from the actuators' array improves the spanwise control authority. It is also demonstrated that the motions within the recirculating domain can be regularized by amplitude modulation of the actuation waveform, thereby inducing large-scale coherent motions that have externally referenced phase and passage frequency, which would make them suitable for adaptive optical corrections.

Nomenclature

b_j	=	actuator orifice width
C_p	=	pressure coefficient
C_μ	=	jet momentum coefficient
D	=	hemisphere diameter
k	=	turbulent kinetic energy
M	=	Mach number
p	=	static pressure
p_s	=	test section static pressure
R	=	hemisphere radius
Re_D	=	Reynolds number
St	=	Strouhal number
U_i	=	i component of the velocity
$\bar{U}_i$	=	i component of the mean velocity
U_j	=	average jet velocity
u_i	=	fluctuation of the i component of the velocity
U_0	=	freestream velocity
γ	=	angle relative to the horizon
γ_a	=	angle of the actuators
γ_s	=	flow-separation angle
ν	=	kinematic viscosity

I. Introduction

THE development of techniques for controlling separation has been driven, since its inception, primarily by the need to accommodate the aerodynamic requirements of airplane flight. Of these, the primary one has been the need to maintain appropriate lift characteristics for takeoff, landing, and in-flight maneuvers. The metric for determining the adequacy of separation control has been the time-averaged lift coefficient, provided that drag is not overly compromised, because the need for controlling separation beyond the flight parameter limits sustained by the nominal geometries of the aerodynamic surfaces exists only during limited portions of the overall mission. The metric becomes much more stringent when separation control is effected for the purpose of enhancing the transmission of optical wave fronts through regions of flow affected by potential separation. When an optical wave front passes through a flow region with variable index of refraction, it becomes distorted or aberrated. Wave-front distortion is created by refraction due to density fluctuations associated with unsteady flows, and therefore reacts to real-time fluid motion. Typical sources of such aberrations are turbulent boundary layers, wakes, and separated shear layers. Separated shear layers are the most significant source of aberrations due to the presence of coherent large-scale vortices, which essentially act as lenses on the optical wave front. Therefore, any optical wave front passing through a separated shear layer would be notably degraded. Applied to aircraft needs, the degradation effect imposes a new requirement on separation control, namely, that the flow-separation point is delayed and, once separated, that inherent formation of coherent motions within the shear layer is suppressed.

The traditional active method for controlling separation behind two-dimensional airfoils makes use of the strong entertainment properties of a shear layer excited at its flapping frequency. Introducing perturbation signals at the nominal (dimensionless) frequency $St = \mathcal{O}(1)$ upstream of the region of separation results in energizing the shear layer to a degree that results in the exhaustion of the air supply between the separated shear layer and the adjacent aerodynamic surface. This effect partially reattaches the separated flow, for a limited time duration, to the aerodynamic surface. Once reattached, the flow responds to the modified pressure gradients along the surface, and separates once more. The cycle of partial reattachment and separation repeats at a rate that is a low integer submultiple of the excitation frequency. Although resulting in a considerable improvement in the mean lift coefficient associated with the affected surface, there is reason to believe that this method would degrade an optical signal being transmitted through the affected region perhaps even beyond the levels observed if control were not applied. However, such an approach may serve as a precursor for an active correction of optical aberrations by means of an adaptive-optics system [1], if the resulting shear layer can be "regularized" by the $St = \mathcal{O}(1)$ active flow control.

A body of work studying the control of separation by the application of perturbation signals at frequencies substantially higher than the flapping frequency of the shear layer suggests that such high-

Received 30 October 2008; revision received 30 April 2009; accepted for publication 15 May 2009.

*Research Engineer, Woodruff School of Mechanical Engineering. Member AIAA.
†Graduate Research Assistant, Woodruff School of Mechanical Engineering. Member AIAA.
‡Professor, Woodruff School of Mechanical Engineering. Associate Fellow AIAA.

frequency excitation makes it possible to achieve attached flows that do not suffer the unsteady effects exhibited by traditional methods [2,3]. Such flows remain continuously attached and the flowfield is free of the degrading optical effects caused by the periodic appearance of highly energized large-scale structures in regions of the flow traversed by optical waves.

Active control of vortex shedding off both aerodynamic and bluff bodies has attracted considerable interest over the years, with research efforts encompassing both passive and active, open- and closed-loop control [4]. A portion of the previous work on separated flows over a three-dimensional configuration has been directly motivated by the aero-optical problems involving an aircraft turret. Such a configuration typically consists of a cylindrical base having a hemispherical cap and a flat or a conformal aperture. The resulting flowfield is fairly complex as shown by de Jonckheere et al. [5]. Attempts to control such flows were performed by examining the effect of suction on the wake structure [6] and by the addition of aft-mounted fairings and splitter plates [7]. The former showed significant alteration of the wake structure even at low levels of suction, while the latter demonstrated reduction of the baseline drag up to 55% using a large fairing. The separated flow behind a turret with a flat aperture and the effects of passive control on the optical aberrations were also addressed and characterized [8], while the aerodynamical and aero-optical characterization of the baseline flowfield over a conformal-window turret configuration was reported recently as well [9]. Vukasinovic and Glezer [10] demonstrated the effectiveness of fluidic, direct high-frequency control on turbulence suppression behind a bluff-body turret at $Re_D = 8 \times 10^5$. Surprisingly enough, there has been almost no work done on the generic configuration of flow over a hemispherical turret, that is, just a surface-mounted hemisphere, besides some motivated by Earth flows over hemispherical domes [11]. Recently, the effectiveness of active high-frequency control in suppression of optical aberrations was demonstrated behind a hemispherical turret at freestream speeds up to $M = 0.5$ [12].

This paper focuses on the basic flow over a hemispherical turret which may be considered as a limit configuration of the widely studied problem of flow over a surface-mounted obstacle having a free end [13]. One classical example of such a problem is the flow over a free-end, surface-mounted circular cylinder [14]. Furthermore, flow over a turret geometry (hemisphere on a cylinder, as described above) may be considered as a circular cylinder problem with a modified free end. A common feature of the separated flows behind any of these surface-mounted obstacles is that the resulting wake-flow topology is dominated by three major vortical sources: at the base of the obstacle, over its main body, and at the free end. The horseshoe vortices which evolve from the front stagnation point may also influence the wake structure. The relative contribution of each of these sources depends on the aspect ratio of the obstacle as well as the specifics of the geometry (flat or profiled free end, circular or noncircular cross section, etc.). Following these general guidelines, the current study can be classified as a problem of flow over a surface-mounted obstacle having zero support thickness and a modified free end. Therefore, it is to be expected that the separated flow is dominated by vortices shed off the "free-end" tip (i.e., the hemispherical cap), and the separated flow at the interface of the cap and the support wall. As noted earlier, such a flow clearly presents challenges to separation control beyond those associated with the separation behind two-dimensional aerodynamic surfaces. Locally, the development of a shear layer at the origin of a separated region off the hemispherical cap is subject to the same instability considerations as that of a two-dimensional flow. The three-dimensional geometry of the surface, which curves not only in the streamwise but also in the lateral direction, subjects the developing spanwise vorticity lines to distortion that makes the overall separation line have the appearance of a horseshoe on the rear of the hemisphere. The present work draws on previous work in similar flow geometry, with the application of actuators using piezoelectric elements operated in the high-frequency mode [10,12] to explore the response of the separated region behind a hemisphere to variations in geometric distribution and harmonic- and modulated-frequency characteristics of an array of actuators.

II. Experimental Setup and Procedures

The present experiments are conducted in an open-return wind tunnel having a test section that measures 91 cm on the side. A hemisphere model is mounted in the bottom wall (the cross-sectional blockage is 4.4%) and is built as a full sphere measuring 30.5 cm in diameter, as shown schematically in Fig. 1. The model is equipped with two rows of individually addressable high-frequency synthetic jet actuators that issue normal to the hemisphere surface. The actuators are mounted side by side along the hemispherical arc where each row has 11 actuator modules mounted flush with the surface. The position of the actuators relative to the horizon (measured by the angle γ_a) can be adjusted. The actuation angle is defined as the angle of the symmetry axis between the two rows such that the synthetic jets actually issue at $\gamma_a - 1.9$ deg and $\gamma_a + 1.9$ deg. Each actuator module consists of a pair of orifices measuring 0.308×18.3 mm and having a spanwise spacing gap of 1.9 mm. The hemisphere is also equipped with 64 pressure ports that are arranged in three rows in the freestream flow direction along the sphere surface in groups of 24, 22, and 18 ports in the central, middle, and outer planes, respectively, as shown in Fig. 1b. The middle plane cuts through the hemisphere at one-third of the radius away from the plane of symmetry, while the outer plane is at two-thirds of the radius. Figure 1c shows a picture of two halves of the full sphere model, with the two arrays of control actuators. The static pressure along the hemisphere surface is measured using a dedicated 64-port PSI Netscanner system. The three pressure profiles are nominally sampled 50 times, and the corresponding averaged profiles are plotted relative to the central plane, such that the same angular position in the plots corresponds to the same distance in the downstream projection of each port. Uncertainty of the averaged pressure measurements is estimated to be less than 1% with a 95% confidence interval.

Piezoelectric actuator modules are custom designed and manufactured, such that their operation range is off resonance of the disk

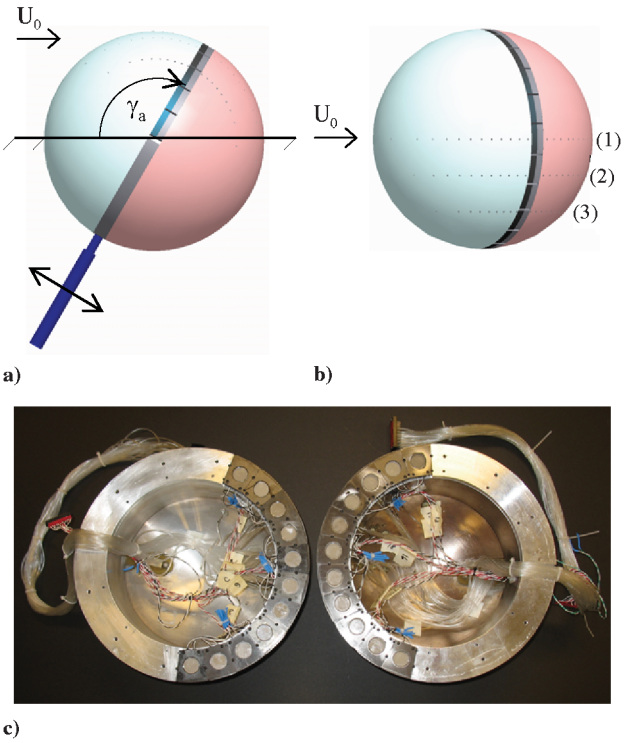

Fig. 1 Shown are the following: a) side view of the hemisphere model with the two actuator rows at an adjustable angle γ_a; b) top view of the hemisphere model showing the three rows of pressure ports in the central (1), middle (2), and outer (3) planes; and c) photograph of the two halves of the sphere model with the two arrays of control actuators.

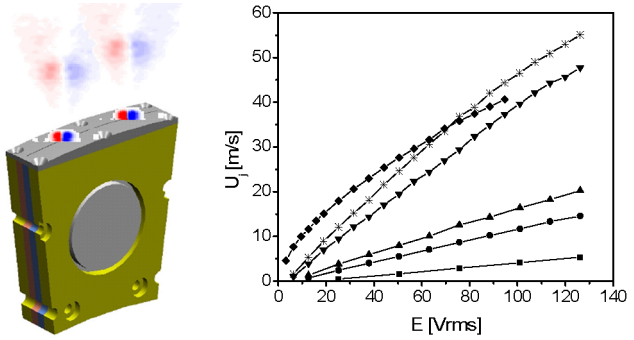

a) b)

Fig. 2 Shown are the following: a) schematics of a single actuator module with overlaid jet vorticity contours measured at the beginning of the actuation cycle; b) average jet exit velocity with voltage input at operating frequencies of $f = 200$ (■), 400 (●), 500 (▲), 1000 (◆), 1600 (▼), and 2000 (*) Hz.

and nominal operation frequency is set to 2 kHz. A schematic of the actuator module is shown in Fig. 2a. To illustrate how the jets are synthesized, jet vorticity raster plots are overlaid on the schematic. Vorticity is extracted from planar particle image velocimetry (PIV) measurements taken in the central plane normal to the jet orifice and phase locked to the sinusoidal actuation signal at $f = 2$ kHz. The actuation phase selected shows the initial stages of the expulsion part of the actuation cycle, which generates two counter-rotating vortices off the orifice boundary. It should be noted that a vortex pair generated by the preceding expulsion is also visible, self-propelled, grown, and diffused as it entrains the surrounding fluid. Farther up, the generated vortices completely lose their coherence, and a jet is established with no "memory" of the harmonic actuation. Before the control application, each actuator module is calibrated in a hot-wire calibration facility by measuring the jet exit velocity at the orifice center, and the average jet exit velocity U_j is defined as a time average over the expulsion part of the actuation cycle. It should be noted that the average jet velocity defined in this way is related to the inverse of the jet Strouhal number $1/St_j = U_j/(2fb_j)$, which is greater than 10 in the present experiments. In addition to the nominal actuation frequency $f = 2$ kHz, jets are calibrated at several lower operating frequencies, and the calibration results are shown in Fig. 2b, showing that average velocities up to $U_j = 55$ m/s can be achieved at the nominal operating frequency. Despite the relatively high voltage required to drive the piezodisks (up to 100 V rms), the low-current operation requires only several watts of power consumption per actuator.

The flow characterization is done such that the baseline flow is first fully established. Once the baseline measurements are complete, the control is activated and, after a delay, the controlled flow is characterized. Such a procedure is clearly motivated by flow control on moving platforms. Planar PIV measurements are taken using off-axis imaging where the camera is mounted on a two-axis computer-controlled traverse. The flow is characterized within the plane of symmetry, which also includes the 24 pressure ports of the central plane. The full field of view that is mapped by PIV measurements is composed of individual, partially overlapping (typically nine) high-resolution windows that span the domain from upstream of the separation off the hemisphere surface up to the reattachment region of the separated flow. A layout of these measurement windows is shown in Fig. 3, where the actual snapshots are imported at their corresponding locations and both the hemisphere surface and the horizontal wall are visible (one of the actuator modules from the downstream row is also seen in window 1). The uncertainties in the directly measured PIV parameters are based on the analysis performed by Adrian [15] and Westerweel [16] and standard statistical analysis for a 95% confidence interval. Uncertainty in the mean streamwise and cross-stream velocities out of 500 samples is estimated to be 3 and 4%, respectively. The spectral content of the flowfield is characterized by hot-wire measurements of the velocity

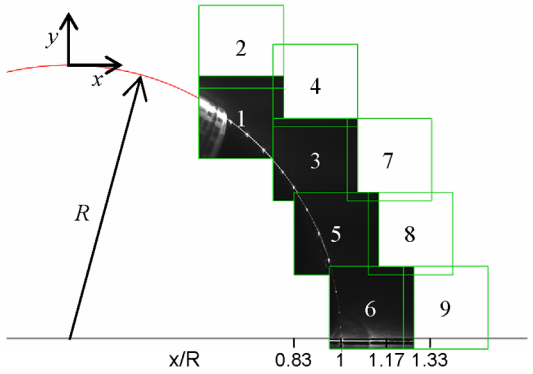

Fig. 3 PIV measurement domain (nine partially overlapping windows). Hot-wire measurement stations are at $x/R = 0.83$, 1, 1.17, and 1.33.

fluctuations measured at four downstream locations $x/R = 0.83$, 1, 1.17, and 1.33 in the vertical central (symmetry) plane, as marked in Fig. 3. Each set of measurements consisted of 100 samples of time traces that yielded 1.8 Hz resolution in the frequency domain. Uncertainty in a single spectral energy distribution is estimated following [17], whereas the uncertainty of the averaged spectral distribution is estimated to be 4% with 95% confidence interval. Because the flowfield changes between the controlled and uncontrolled cases, the velocity fluctuations are measured at the cross-stream locations that correspond to $\bar{U} = U_0/3$, $U_0/2$, and $2U_0/3$ for a given flow.

The present data are obtained for $Re_D = 404,000$–$706,000$ ($U_0 = 20$–35 m/s), Strouhal number $St = fD/U_0 = 17.4$–30.5, and jet momentum coefficient, defined as $C_\mu = \rho U_j^2 A_j/(\rho U_0^2 A_0) = 0.75 \times 10^{-2}$–$2.3 \times 10^{-2}$, where A_j is the total jet orifice area and A_0 is the frontal projection area of the turret. It should be noted that the turret's oncoming wall boundary layer is substantially lower than the hemisphere radius, as the front stagnation point in the central plane is measured at 12 deg elevation angle at the highest Re_D baseline flow. Furthermore, local boundary layer thickness at the hemisphere apex is measured at 6 mm for the same baseline flow. The actuators are nominally positioned at $\gamma_a = 120$ deg, except when stated otherwise. Both rows of actuators are operated simultaneously in the controlled cases.

The present work explores the response of separated flow behind the turret region to variations in actuation parameters. All measured parameters are made nondimensional using the turret radius $R = D/2$ as a length scale, and R/U_0 as the time scale, while pressure data are shown in terms of the pressure coefficient $C_p = 2(p - p_s)/\rho U_0^2$, where p_s is the static pressure in the test section freestream. The baseline flow is discussed in Sec. III. The effects of direct high-frequency actuation at Reynolds numbers up to 706,000 are discussed in Sec. IV. The addition of indirect large-scale excitation to direct small-scale actuation is described in Sec. V. Benefits of deliberate tripping of the upstream flow on flow control effects are discussed in Sec. VI, while Sec. VII summarizes conclusions of the present work.

III. The Baseline Flow

Figure 4 shows cross-stream distributions of the mean velocity and vorticity concentrations within the central meridional plane for the baseline (unforced) flows at $Re_D = 4.04 \times 10^5$, 5.05×10^5, 6.06×10^5, and 7.06×10^5. The angular location of the inactive actuators is marked by a gray arrow. The recirculating region is clearly resolved in these measurements and it indicates a relatively short ($x/R \approx 1.4$–1.6) reattachment length of the separated flow. The strength of the recirculating core of the separated region increases with Re_D. An upstream shift of the recirculating core with the increase in Re_D is induced by a corresponding upstream shift of separation in this plane. The static pressure distributions that correspond to the flowfields in Figs. 4a–4d are shown in Fig. 5. The pressure profiles in the central plane (Fig. 5a) indicate that the

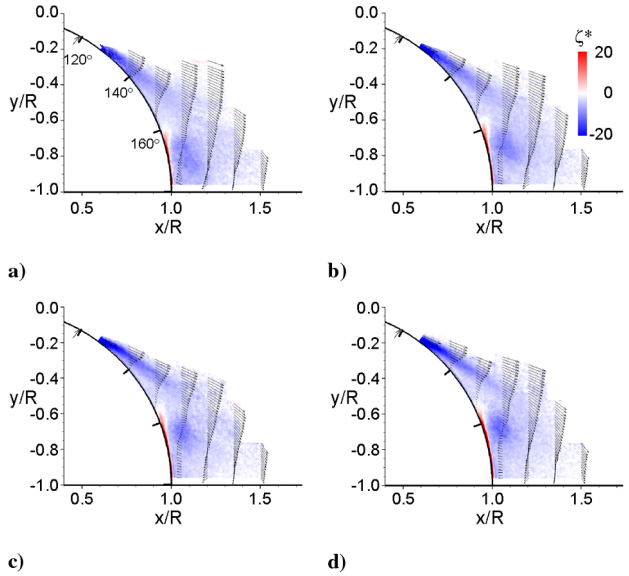

Fig. 4 Raster plots of the mean vorticity ζ^* and velocity profiles for the baseline (unforced) flow: a) $Re_D \times 10^{-5} = 4.04$, b) 5.05, c) 6.06, and d) 7.06.

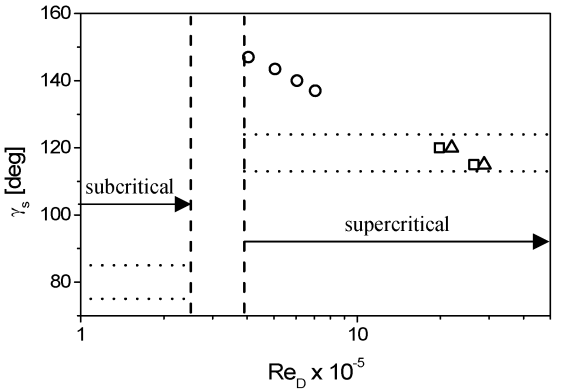

Fig. 6 Separation angles along the axis of symmetry for the baseline flow (○) and for the hemispherical (□, [12]) and hemisphere-on-cylinder (△, [9]) turret.

separation (seen as a sudden drop in pressure recovery) at $Re_D = 7.06 \times 10^5$ occurs at $\gamma_s \approx 135$ deg, and that γ_s increases as Re_D decreases, exceeding 140 deg for $Re_D = 4.04 \times 10^5$. The accompanying pressure distributions along the middle plane are shown in Fig. 5b, whereas the outer plane profiles are shown in Fig. 5c; as noted in Sec. II, the pressure distributions are projected onto the central plane and shown relative to the central angular position γ. The pressure distributions along the middle and outer planes show that the flow separates first in the outer plane and the separation in the middle plane occurs farther downstream such that the difference in the angular position of the separation point is between 5 and 10 deg, while the flow remains attached the farthest in the central plane. Therefore, from the standpoint of the normal projection of the separation line (top view), these pressure distributions suggest that the separation line across the hemisphere surface is shaped as a streamwise horseshoe, and that the onset of separation is close to the spanwise intersection between the hemisphere and the horizontal surface. Furthermore, it appears that the pressure distribution in the outer row is the least affected by the recirculating flow domain, which is indicated by nearly uniform pressure profiles past the separation point. Therefore, the recirculating domain is nested in the central region behind the turret and does not extend across the full turret span.

Figure 6 shows the variation of the separation angle in the central plane with Reynolds number, along with the three characteristic separation domains for the case of a free sphere [18]. The subcritical domain is characterized by laminar boundary layer separation off the forward surface of the sphere, at about 80 deg, whereas the supercritical domain is characterized by turbulent boundary-layer separation off the aft surface of the sphere. A narrow critical region is denoted by the dashed lines, where the boundary-layer transition makes the flow susceptible to local separation that is immediately followed by reattachment. Once the flow is reattached, full separation is delayed in the downstream direction. When the flow becomes turbulent in the supercritical domain, the separation angle is about 120 deg. As shown in Fig. 6, the separation angles of the present experiments fall just outside of the critical regime for the free sphere. However, there are two major differences between the flow separation about the present hemisphere and that of a free sphere. First, the front stagnation point on the hemispherical turret, which depends on thickness of the upstream boundary layer, is displaced downstream by about 12 deg in the central plane. Second, the global flow dynamics and separation are influenced by the necklace vortices that form at the juncture between the hemisphere and the support surface, and their sense is such that high-momentum fluid is transported toward the central hemisphere surface, thus contributing the separation delay. It is conjectured that these effects result in a shift of the critical separation regime toward higher Reynolds numbers, and therefore the present separation angles fall within the critical (rather than supercritical) domain. The relatively high separation angles are therefore attributed to the presence of small separation bubbles that spatially precede the full separation. Taneda [19] noted that for a critical flow over a free sphere at $Re_D = 3.5 \times 10^5$, "delayed" separation at 135 deg was preceded by "premature" separation at 110 deg. Similarly, the separation angle within the critical domain of the flow over a cylinder can exceed 140 deg [20]. Snyder et al. [7] studied the flow over a vertical cylinder supporting a hemispherical cap at a similar range of Reynolds numbers as in the present study, but at higher freestream velocities. These authors found that separation near the spanwise edges precedes the separation on the top of the turret, but their pressure measurements lack the resolution necessary

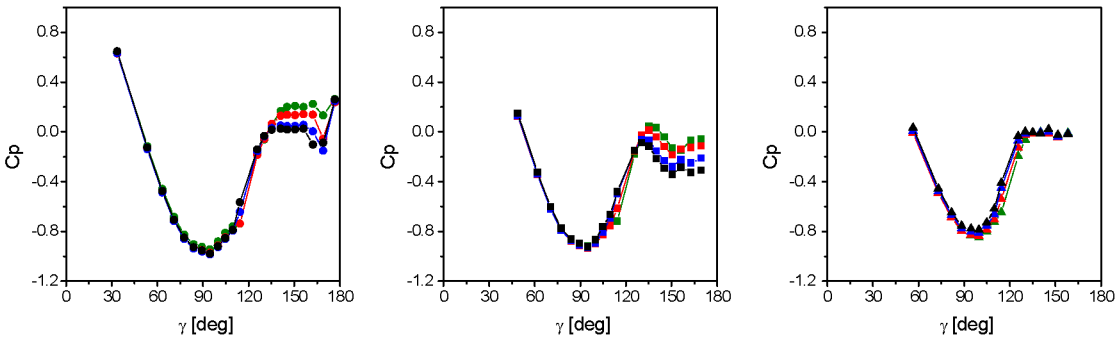

Fig. 5 Static pressure profiles for the baseline flow at $Re_D \times 10^{-5} = 4.04$ (green), 5.05 (red), 6.06 (blue), and 7.06 (black): a) central, b) middle, and c) outer planes. Pressure levels decrease with an increase in Re_D.

to assess the separation angle in the central plane. Still, the central static pressure profile indicates that separation does not occur below 130 deg. Other studies documented separation angles at Reynolds numbers of the order of 10^6, which are also shown in Fig. 6. Gordeyev et al. [9] reported that flow separation off a hemispherical cap on a cylinder occurs just downstream of $\gamma_s = 120$ deg for $M = 0.3$, and continuously decreases with increasing M (up to $M = 0.45$), to about $\gamma_s = 115$ deg. Vukasinovic et al. [12] reported that the central plane separation angle for a hemispherical shell mounted on a flat plate shifts upstream from $\gamma_s = 120$ deg to 115 deg as the freestream Mach number increases from $M = 0.3$ to 0.5. All of the cases at $Re = \mathcal{O}(10^6)$ clearly fall into the supercritical separation domain, and there is good agreement between the separation angles in these tests and the corresponding data for the free sphere (Fig. 6).

IV. Harmonic High-Frequency Control

The effect of high-frequency actuation ($\gamma_a = 120$ deg) is demonstrated in Fig. 7 for $Re_D = 4.04 \times 10^5$ ($St = 30.5$ and $C_\mu = 2.3 \times 10^{-2}$) and $Re_D = 6.06 \times 10^5$ ($St = 20.3$ and $C_\mu = 1.02 \times 10^{-2}$). The angular location of the actuators is marked by a red arrow, and the inset plot illustrates the shape of the actuation signal. The corresponding baseline cases are shown in Figs. 4a and 4c, respectively. The controlled flowfield in the central meridional plane is dramatically altered at $Re_D = 4.04 \times 10^5$ (Fig. 7a). As a result of the actuation, the flow remains attached to the surface for approximately 20 deg farther downstream compared to separation in the absence of control, and only a small recirculating bubble is formed above the juncture between the hemisphere and the surface. Consequently, the flow effectively reattaches immediately downstream of the hemisphere. The high-frequency actuation also shows a significant control authority at $Re_D = 6.06 \times 10^5$ (Fig. 7b), even as C_μ is effectively halved. The separation point is again pushed about 20 deg, and the recirculating core is concentrated around the vicinity of the juncture with the surface (cf. Fig. 4c) so that the reattachment point is moved upstream to $x/R = 1.35$ from $x/R = 1.4$. The accompanying pressure distributions for the controlled flows are shown in Fig. 8 along with the corresponding baseline profiles. In either case, the effect of the high-frequency forcing is the most prominent along the central plane. This may be attributed to the fact that the flow separates farther upstream near the spanwise edges and therefore the relative distance of the actuators from the separation line varies from the central to the outer plane. It is noteworthy that even though the actuators are located at $\gamma_a = 120$ deg, the actuator jets modify the flow and surface pressure both upstream and downstream of γ_a. Upstream from the actuators the local velocity near the hemisphere surface begins to increase (relative to the baseline) at about $\gamma = 70$ deg, as is evidenced by the lower static pressure. This trend continues downstream of the actuators as the pressure continues to recover past the unforced separation point and the flow remains attached longer. It should be noted that for $Re_D = 4.04 \times 10^5$, the effect shown in Fig. 7a could also be achieved with a single row of actuators, that is, at half the jet momentum coefficient.

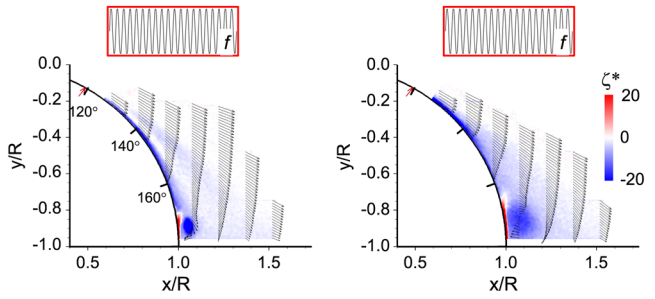

Fig. 7 Raster plots of the mean vorticity ζ^* and velocity profiles for the controlled flowfields ($\gamma_a = 120$ deg): a) $St = 30.5$ and $C_\mu = 0.023$, and b) $St = 20.3$ and $C_\mu = 0.010$ using harmonic actuation. The corresponding baseline flows are shown in Figs. 4a and 4c.

The effects of the actuation are investigated in more detail at the highest Reynolds number of the present work, $Re_D = 7.06 \times 10^5$. First, the optimal actuation angle is sought within the range 80 deg $< \gamma_a <$ 140 deg using both pressure and PIV measurements. Because the main segment of the recirculating domain of the baseline flow (Fig. 4d) is located within the window labeled as 5 of the measurement domain (cf. Fig. 3), the PIV measurements are conducted within this single window and the resulting flowfields are shown in Fig. 9 as raster plots of vorticity with overlaid streamlines. It should be noted that the actuator location is always upstream of this window for all γ_a that are tested. Figure 9a shows the baseline flowfield for reference. When the actuation is applied at $\gamma_a = 80$ deg, the core of

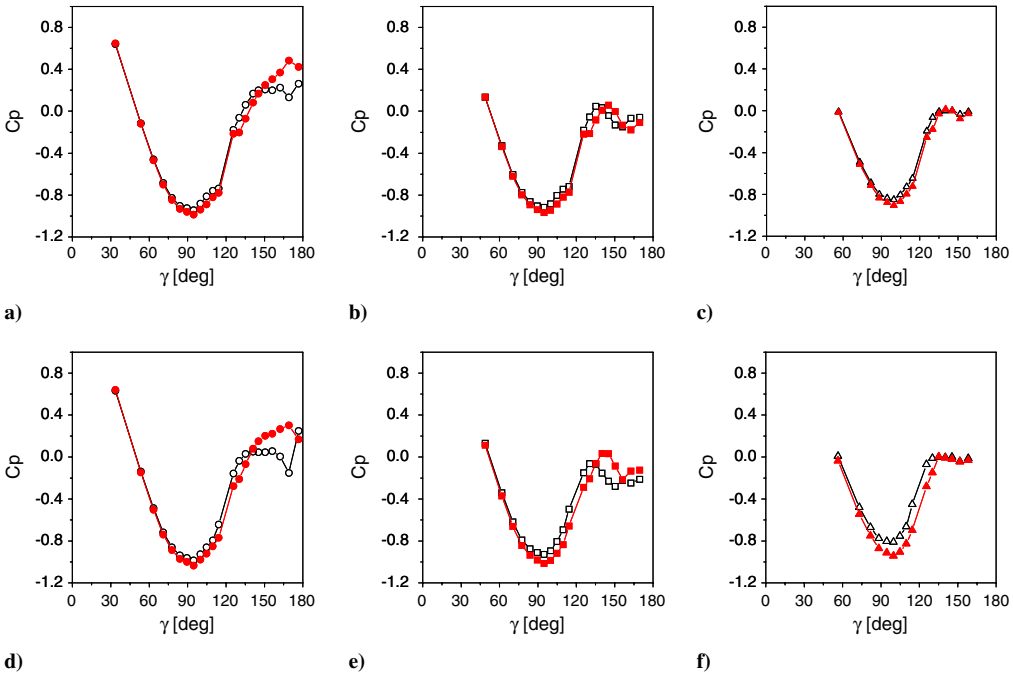

Fig. 8 Static pressure distributions for the baseline (open symbols) and controlled (as in Fig. 7, solid symbols) flows: a, d) central planes, b, e) middle planes, and c, f) outer planes (cf. Fig. 1); a–c) $Re_D \times 10^{-5} = 4.04$, and d–f) 6.06.

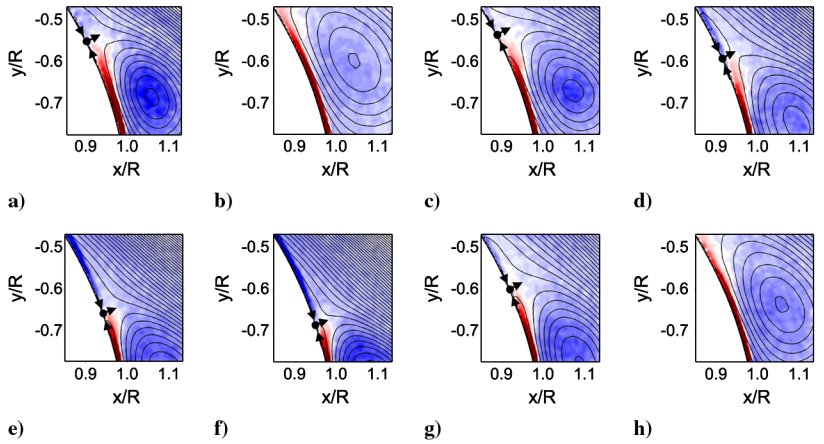

Fig. 9 Raster plots of the mean vorticity ζ^* with overlaid streamlines for $Re_D = 7.06 \times 10^5$ and $C_\mu = 0.0075$ (window 5, Fig. 3): a) baseline flow, b) $\gamma_a = 80$ deg, c) 90 deg, d) 100 deg, e) 110 deg, f) 120 deg, g) 130 deg, and h) 140 deg.

the recirculating region moves upstream relative to the baseline case. The actuation apparently induces a premature separation and, as a consequence, the separated region increases in size as is evidenced by the decrease in the intensity of the vorticity concentrations as the circulation domain broadens. As γ_a increases, the separation moves downstream and for $\gamma_a = 100$ deg (Fig. 9d), the separation is farther downstream ($\sim$155 deg) than in the baseline flow. Note that the present measurements do not show whether for $\gamma_a < 90$ deg there is possibly a reattachment domain downstream of the actuators that could be followed by a secondary separation. However, once the actuation is applied where the pressure gradient on the surface of the hemisphere is adverse, the virtual displacement induced by the actuation results in delay of separation. The separation is pushed farther downstream for $\gamma_a = 110$ and 120 deg to past 160 deg (Figs. 9e and 9f). Beyond that, $\gamma_a = 130$ and 140 deg result in upstream motion of the separation (Figs. 9g and 9h). It appears that the adverse effects of actuation at angles that are near or beyond the separation point of the baseline flow in the plane of symmetry (e.g., Figs. 9g and 9h) are related to the fixed jet momentum coefficient and resulting jet penetration into the outer flow. In the case of actuation upstream from the separation (Fig. 9g), the flow is effectively forced to fully separate at the point where the jets are issued. As the jet can penetrate the already separated flow even stronger at $\gamma_a = 140$ deg (Fig. 9f), its effect becomes even more detrimental as the outer flow is forced to separate farther upstream. These data also demonstrate that for a given (fixed) C_μ, there is an optimal location of the jets for maximum separation delay which, for the present conditions, is $\gamma_a = 120$ deg corresponding to the dimensionless actuator location $s^* = (\gamma_a - \gamma_s)/180 \text{ deg} = -0.083$. This actuator location is used in the remainder of the present experiments. Alternatively, for a given actuation angle C_μ, there should be an optimal C_μ for the most favorable flow-separation delay.

The full nine-window PIV measurements of the baseline and controlled flowfields at $Re_D = 7.06 \times 10^5$ are shown in Fig. 10. Figures 10a and 10b are raster plots of vorticity concentrations with overlaid velocity distributions of the baseline and controlled ($St = 17.4$ and $C_\mu = 0.75 \times 10^{-2}$) flows, respectively. As shown in Fig. 9, the controlled flow remains attached for $\sim$14 deg farther than the baseline flow, which is indicated by the strong boundary-layer vorticity along the hemisphere surface (Fig. 10b). This separation delay in the central plane is accompanied with a strong reduction in the near-wall velocity deficit, as a consequence of the vectored outer flow toward the hemisphere surface. The delay in separation is also accompanied by a reduction in the extent of the recirculating flow domain and in the reattachment distance. In addition, the (clockwise sense) vorticity becomes concentrated in the juncture between the hemisphere and supporting surface. The flows are also characterized by distributions of a two-dimensional estimate of the turbulent kinetic energy $k = \bar{u}^2/2 + \bar{v}^2/2$ (Figs. 10c and 10d). The baseline flow (Fig. 10c) has relatively high concentrations of kinetic energy both in the separating shear layer and within the recirculating core, which delineate regions of high mixing. It is remarkable that when the actuation is applied, the overall level of kinetic energy in the separated region is significantly reduced (Fig. 10d). In particular, the peak kinetic energy in the core of the recirculating domain is lower than half the corresponding level in the baseline flow and turbulent kinetic energy within the separating shear layer is barely visible within the same magnitude range. Although it might be argued that the delay in separation and reduction in the extent of the recirculating domain lead to the reduction of the turbulent kinetic energy, previous work suggests that this is not the only mechanism that leads to suppression of the fluctuating energy. However, a static control effect such as separation delay is inherently reflected in the turbulence suppression within the wake, and it is virtually impossible to separate two mechanisms. Vukasinovic et al. [21] showed that direct high-frequency flow control of shear layers induces active disruption of the turbulent kinetic energy budget via dissipative mechanisms even in the absence of significant separation delay. In that work, the separation line was kept fixed, and subsequent alteration of the baseline shear layer was decoupled from the effect of separation delay. Similarly, even when the global scale of the recirculating region in the present study is not significantly diminished by the high-frequency forcing (e.g., actuation with low C_μ, not shown), the turbulent kinetic

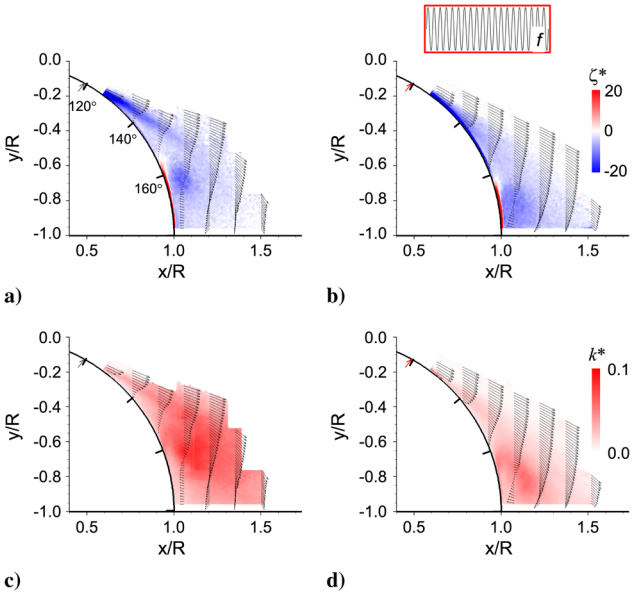

Fig. 10 Raster plots: a, b) mean vorticity ζ^*, and c, d) turbulent kinetic energy k^* at $Re_D = 7.06 \times 10^5$ for the baseline (a, c) and the controlled (b, d, $\gamma_a = 120$ deg, $St = 17.4$, and $C_\mu = 0.0075$) flows.

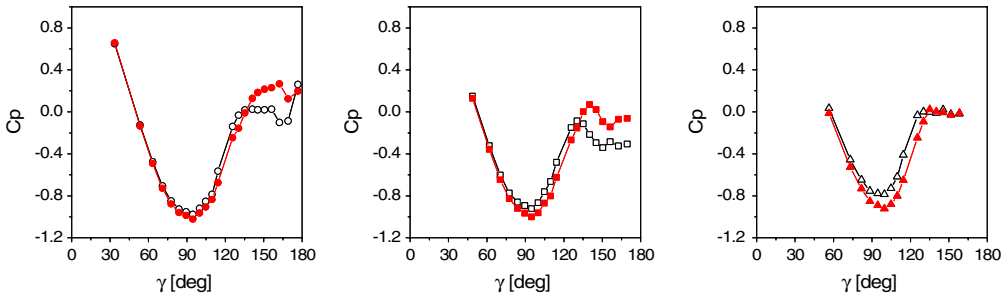

Fig. 11 Static pressure distributions for the baseline (open symbols) and controlled (as in Fig. 10, solid symbols) flows for $Re_D = 7.06 \times 10^5$: a) central planes, b) middle planes, and c) outer planes.

energy within the separated region still decreases relative to the uncontrolled flow. It is thus argued that the high-frequency forcing leads to enhanced dissipation and therefore has a stabilizing effect on the separated flow in addition to that caused by the delay of separation. Similar effects were observed in other shear layer flows [21–23] where it was shown that high-frequency actuation suppresses the large-scale motions. Such an effect was attributed [21] to increased dissipation of turbulent kinetic energy in the near field, which is followed by reduction in its production farther downstream. Distributions of the static pressure corresponding to Fig. 10 are shown in Fig. 11. As seen with the lower Reynolds-number flows (Fig. 8), the effect of the forcing is strongest in the central plane. Note also the drop in pressure in the middle plane following separation in the absence and presence of actuation. This may be attributed to the effect of the recirculating core that induces higher velocities near the middle plane. Also, the relative change in pressure (and therefore in the local velocity) before separation increases from the central to the outer plane. Therefore, the largest relative increase in local velocity induced by the actuation is in fact in the outer plane even though the least effect on the location of separation is realized there.

The PIV-based estimates of the turbulent kinetic energy (Figs. 10c and 10d) do not distinguish between the different flow scales. Therefore, this information is assessed from spectral measurements using single-sensor hot-wire anemometry (cf. Sec. II) at $x/R = 0.83$, 1, 1.17, and 1.33. At each of these four downstream stations, measurements are taken at the cross-stream elevation y at which the time-averaged streamwise velocity $\bar{U}$ is equal to $U_0/3$, $U_0/2$, and $2U_0/3$. Therefore, as the structure of the recirculating flow domain is altered in the presence of actuation, the cross-stream (y) elevations are below the corresponding elevations in the baseline (uncontrolled) flow. As an example, the power spectra corresponding to $U_0/2$ are shown in Fig. 12. Figure 12a shows the baseline and controlled power spectra at the measurement station that is closest to the actuators ($x/R = 0.83$). The baseline spectra exhibit a rather broad low-frequency peak at about $f = 16$ Hz, which corresponds to the Strouhal number $St = 0.144$. This Strouhal number is within the range of the Strouhal numbers that characterize the wake frequencies of full spheres or cylinder/hemisphere turret configurations. For instance, Purohit et al. [6] measured a shedding frequency that corresponds to $St = 0.226$ at $M = 0.6$ for the flow over a three-dimensional turret, whereas a somewhat lower shedding frequency was reported at $St = 0.2$ for a full sphere [24]. Gordeyev et al. [9] reported the turret wake shedding frequency at $St = 0.35$ for any $M = 0.3$–0.45. In the presence of actuation, the spectrum at $x/R = 0.83$ exhibits substantially lower energy in the large scales while the energy magnitude of the spectral components at the small scales is comparable or slightly lower than in the baseline flow with a strong peak at the forcing frequency. It is significant that in spite of the local addition of the turbulent kinetic energy through the actuation, the added energy quickly dissipates and appears to diminish before the first measurement station. Although the low-frequency peak seen in the baseline flow disappears in the power spectrum of the controlled flow, there is a rather broad range of scales (up to $f = 100$ Hz) with relatively high energy even in the controlled flow. The largest spectral suppression in the controlled flow is evident between 100 and 1000 Hz. At the next streamwise station $x/R = 1$ (Fig. 12b), the difference in energy between the controlled and uncontrolled flows is further augmented. Compared to the baseline flow, there is at least an order-of-magnitude decrease in the energy of a broad range of large-to-moderate scales in the presence of actuation. Even though there is still a strong peak at the actuation frequency, there is a further decrease in the magnitude of spectral components at higher frequencies. At the next station $x/R = 1.17$ (Fig. 12c), the peak at the forcing frequency is indistinguishable from the background levels. The difference between the power spectra of the baseline and controlled flow widens across all scales, with the strongest effect at the low frequencies. Finally, the same trend is continued at the last downstream station at $x/R = 1.33$ (Fig. 12d), which exhibits the largest overall suppression as compared to the baseline.

V. Amplitude-Modulated Control

Optical aberrations due to the strong coherent motions can be corrected by adaptive optical techniques [1], where an array of small individually actuated mirrors is driven to unwarp the distortion induced at the passing frequency of the vortices. In such a case, it is desirable that the vortical motions and their passage frequency are the least distorted, that is, that they are regularized. If such an objective is

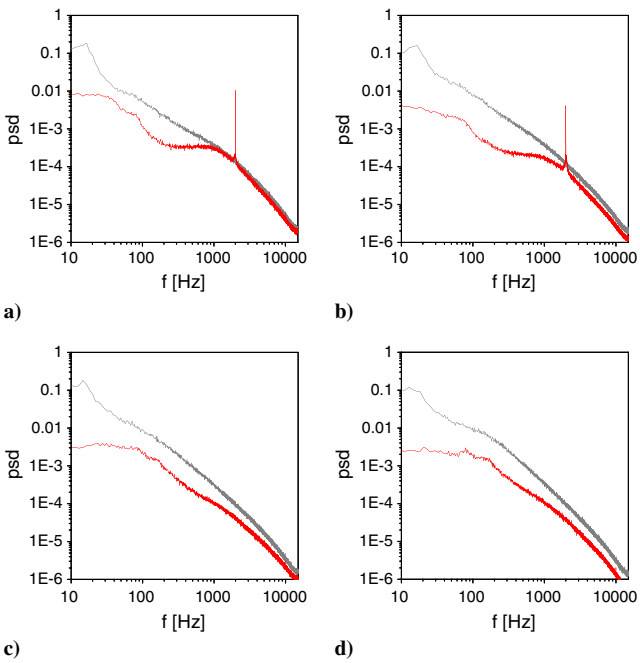

Fig. 12 Power spectra of the velocity fluctuations for the baseline (gray) and controlled (as in Fig. 10, dark, red color) flows at $Re_D = 7.06 \times 10^5$: a) $x/R = 0.83$, b) 1, c) 1.17, and d) 1.33.

sought, the high-frequency control input has to be modified. Rather than applying optical corrections by adaptive optics relative to the natural shedding frequencies, it would be preferable that those large-scale coherent motions are induced by an external source having prescribed frequency and phase. Wiltse and Glezer [25] showed that amplitude modulation of the high-frequency actuation in plane shear layers induces large coherent vortical structures at the modulation frequency and that such structures can, in fact, supersede the natural vortices. A similar approach is tested in the present experiments, in which high-frequency actuation is applied at $Re_D = 7.06 \times 10^5$. Instead of being a time-harmonic signal, the actuation waveform is amplitude modulated by a square wave at $f_{\mathrm{AM}} = 100$ Hz with 50% duty cycle, which essentially renders the high-frequency actuation active only during the first half of the modulation period and inactive during the second half, such that the momentum coefficient of the synthetic jets is effectively halved. It should be noted that even in the case when the jet momentum coefficients of the harmonic and amplitude-modulated control are matched, it is not expected that the resulting effects of the control would be the same. As shown by Vukasinovic and Glezer [26], application of amplitude-modulated high-frequency control combines the effects of both small- and large-scale manipulation of the shear layer (separated flows), and additional large-scale entrainment is excited along with the small-scale mixing.

The flowfield in the presence of amplitude-modulated actuation is first characterized in terms of the ensemble-averaged velocity, vorticity, and turbulent kinetic energy fields (Fig. 13). Compared to the baseline flow (Fig. 10a), the amplitude-modulated control does not alter the location of the separation point significantly. However, the main difference is manifested in the shift of the recirculating core, which is moved downstream to the juncture between the hemisphere and the plate (similar to the results shown in Fig. 10b). Comparison of the turbulent kinetic energy distribution in the presence of amplitude-modulated actuation (Fig. 13b) with the baseline field (Fig. 10c) shows a notable reduction in the maximum levels of k which is consistent with the previous (harmonic actuation) cases. Although the separated domain does not change significantly with modulated actuation, the levels of turbulent kinetic energy distribution are reduced over the domain ostensibly owing to the dissipative effects of the high-frequency actuation. The corresponding static pressure distributions are shown in Fig. 14 along with the pressure distributions of the baseline flow. The pressure distributions in all three planes further support the conclusion that the actuation has a weaker effect on the separation delay compared to the harmonic high-frequency actuation (Fig. 11). However, it should be noted that the pressure levels within the separated regions in all three planes are comparable indicating more spanwise coherence (or less difference in the local velocity distributions) in the separated region at these spanwise locations than was evident without amplitude modulation. This effect is especially pronounced in the middle plane (Fig. 14b) that previously showed a significant pressure drop in the separated domain (cf. Fig. 11b). Accompanying spectral analysis of the amplitude-modulated flow is shown in Fig. 15, characterized in the same manner as for the harmonic high-frequency actuation (Fig. 12). There are two noteworthy features. First, the spectral peaks at the modulation frequency (demodulated from the actuation input) are strong at all streamwise locations, which suggests the presence of spanwise-coherent motions. Second, in spite of the local addition of energy at the actuator location, there is a clear decrease in energy across all scales, except at the forcing and modulation frequencies and their harmonics. Although the decrease in energy is not as pronounced as in the case of the harmonic high-frequency actuation, it is still significant and in accordance with the halved jet momentum coefficient. Furthermore, as the flow evolves in the downstream direction, the effect of the higher harmonics of the modulation frequency diminishes along with the dissipation of the high-frequency peak of the carrier signal and its sidebands, so that the only coherent peak detected at the last downstream location $x/R = 1.33$ (Fig. 15d) is that of the modulation frequency, where coherent motions at this frequency dominate the flow. Finally, an integral measure of the spectral energy alteration by the control input is shown in Fig. 16. Measured spectral energy distributions by the hot wire are integrated across all the scales (frequencies) at each measurement location and for the baseline, harmonic, and amplitude-modulated control input. The results are shown as a relative measure of the integrated energy of the controlled flow P and the energy in the corresponding baseline flow P_b. Figure 16a illustrates the overall energy suppression by the harmonic high-frequency actuation. There is a clear trend of enhanced suppression of energy across the separated flow, with the magnitude of energy suppression related to the proximity to the shear layer: the closer the measurement point is to the high-speed flow zone at any downstream location, the more the energy suppression is pronounced. Thus, approximately an order-of-magnitude suppression is measured at cross-stream locations where local $\bar{U}$ is $2U_0/3$. Still, even in the low-speed region of the flow ($\bar{U} = U_0/3$), a sevenfold reduction in energy is measured. As expected from the analysis related to Fig. 16b, the analogous analysis of the amplitude-modulated control case yields lower overall suppression of the fluctuating energy. The same trend of the highest suppression in the high-speed region of the flow is detected, only in this case the integrated energy is about 7 times lower than in the baseline flow, whereas a threefold reduction is measured in the low-speed region.

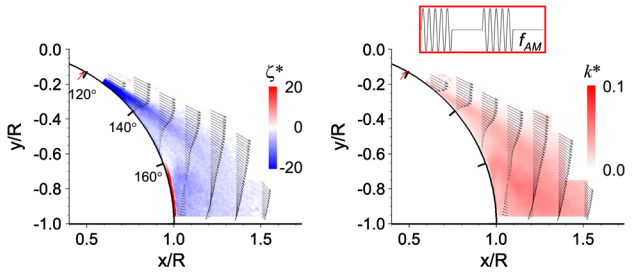

Fig. 13 Raster plots at $Re_D = 7.06 \times 10^5$ with amplitude-modulated control applied at $\gamma_a = 120$ deg, $St = 17.4$, $St_{\mathrm{AM}} = 0.87$, and $C_\mu = 0.00375$: a) mean vorticity ζ^*, and b) turbulent kinetic energy k^*.

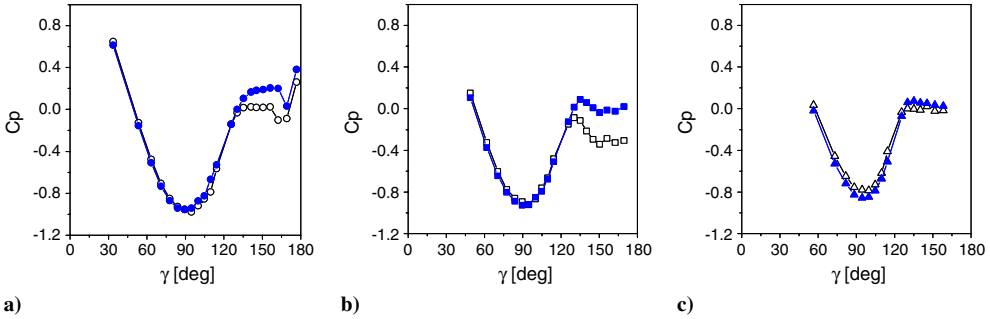

Fig. 14 Static pressure distributions for the baseline (open symbols) and controlled (as in Fig. 13, solid symbols) flows in the a) central, b) middle, and c) outer planes for $Re_D = 7.06 \times 10^5$.

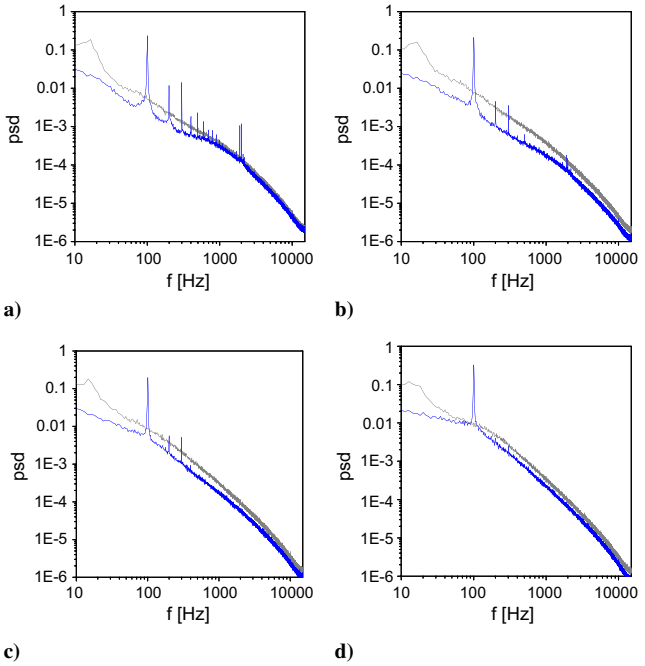

Fig. 15 Power spectra of the velocity fluctuations for the baseline (gray) and controlled (as in Fig. 13, dark, blue color) flows at $Re_D = 7.06 \times 10^5$: a) $x/R = 0.83$, b) 1, c) 1.17, and d) 1.33.

VI. High-Frequency Control of Tripped Separation

As discussed in connection with Fig. 8, the spanwise-nonuniform effect of the high-frequency control in the three planes in which the static pressure is measured may be in part attributed to the fixed spanwise distribution of actuators and uneven spanwise separation across the hemisphere. In fact, as noted above, because the actuators are aligned along an arc and the separation line appears in the shape of a streamwise horseshoe, the actuation distance from the separation line, and therefore control effectiveness, changes along this arc. To assess the impact of the uneven distance from the control input to the local separation point, the distance of the actuators from the separation line is forced to be uniform by inducing a deliberate separation just upstream of the actuators using a 0.89-mm-diam trip wire that is placed along an arc at $\gamma = 118$ deg in the central plane, that is, by forcing the flow separation to occur 2 deg upstream from the actuators along the whole span.

The static pressure distributions for the tripped flow in the absence and presence of actuation at $Re_D = 7.06 \times 10^5$ are plotted in Fig. 17. The corresponding pair of baseline and actuated pressure profiles for the nontripped flow is shown in Fig. 11. The distributions in the absence of actuation in the three measured planes indicate that, as a result of the presence of the trip, the flow indeed separates evenly across the hemisphere. When the actuation is applied, its effect on the delay of separation is more uniform within the three measurement planes than in the corresponding nontripped case, but the effect is still stronger along the central plane and weaker at the spanwise edges. Figure 18 summarizes separation delay effects achieved in the three measurement planes with harmonic control at four Reynolds numbers, and both amplitude-modulated and harmonic control of the tripped flow at $Re_D = 7.06 \times 10^5$. Although still nonuniform in the spanwise separation delay, flow control of the tripped baseline flow shows an improvement in both magnitude and spanwise extent of the separation delay relative to the nontripped baseline flow. It is anticipated that the remaining nonuniformity can be further reduced by applying a spanwise-nonuniform distribution of the actuation strength; however, achieving a fully uniform effect of the flow control across the hemisphere always remains tempered by the underlying three dimensionality of the flow.

Distributions of the velocity, vorticity, and turbulent kinetic energy fields for the tripped, uncontrolled, and controlled flows are shown in Fig. 19. The corresponding flowfields for the nontripped case are shown in Fig. 10. The vorticity concentrations in the absence of

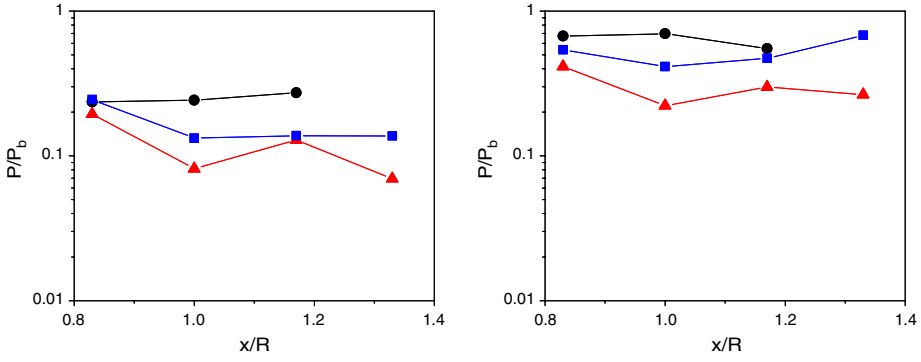

Fig. 16 Ratio of the integrated spectral energy of velocity fluctuations for the controlled and the baseline flows at $U/U_0 = 1/3$ (●), 1/2 (■), and 2/3 (▲) at $Re_D = 7.06 \times 10^5$, $\gamma_a = 120$ deg, and a) $St = 17.4$, and $C_\mu = 0.0075$, b) $St_{AM} = 0.87$, and $C_\mu = 0.00375$.

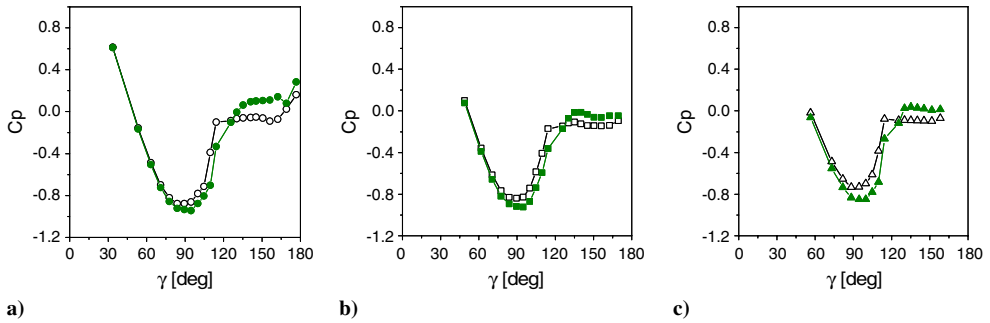

Fig. 17 Static pressure distributions for the baseline (open symbols) and controlled (solid symbols) flow at $Re_D = 7.06 \times 10^5$ ($\gamma_a = 120$ deg, $St = 17.4$, and $C_\mu = 0.0075$) for the tripped flow: a) central planes, b) middle planes, and c) outer planes.

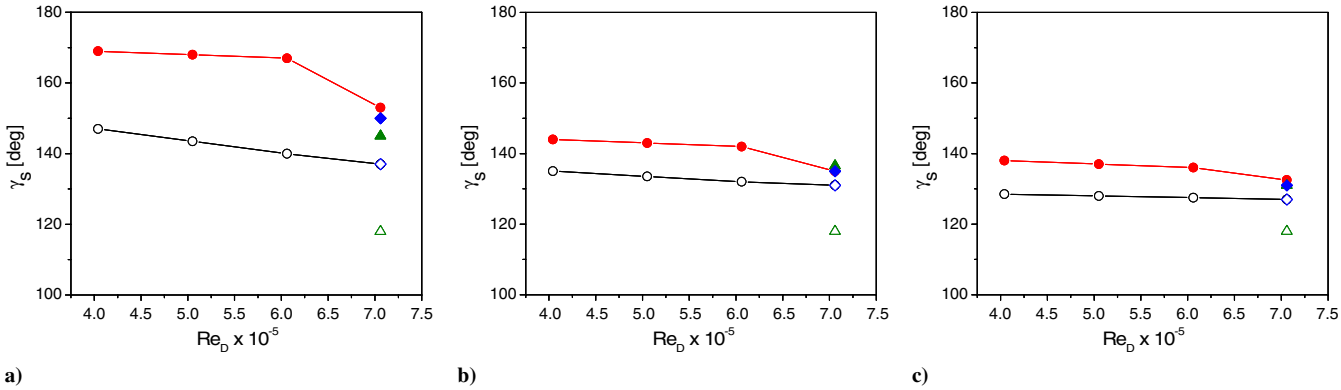

Fig. 18 Separation angles in the baseline (open symbols) and controlled flows (solid symbols) for harmonic (red line, ●), amplitude modulated (blue ◆), and tripped flow (green ▲, △): a) central planes, b) middle planes, and c) outer planes.

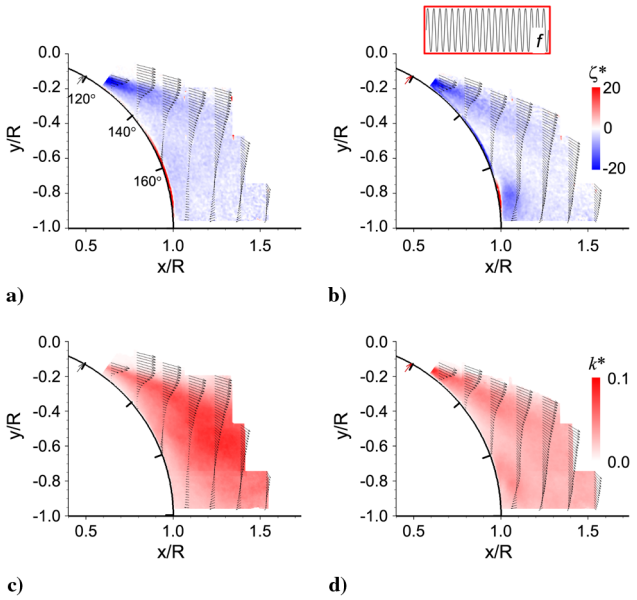

Fig. 19 Raster plots at $Re_D = 7.06 \times 10^5$ for the baseline a), c) and controlled b), d), as in Fig. 17 flows: a, b) mean vorticity ζ^*, and c, d) turbulent kinetic energy k^*.

actuation (Fig. 19a) show strong separation at the trip. Owing to the size of the separated domain, the magnitude of the vorticity is relatively low due to the low velocity induced within the recirculating core. However, when actuation is applied (Fig. 19b), the flow reattaches and a strong vortex forms near the juncture with the base as the recirculating core is displaced downward. The turbulent kinetic energy of the tripped, uncontrolled flow (Fig. 19c) is relatively high throughout the separated domain. When the actuation is applied, there is an overall reduction in the levels of k and the corner vortex is easily distinguishable.

VII. Conclusions

The effectiveness of direct high-frequency control of the separated flow over a hemispherical turret is investigated experimentally for Reynolds numbers between 4×10^5 and 7×10^5 using particle image velocimetry, hot-wire anemometry, and surface pressure measurements. Actuation in the present work is effected at frequencies that are at least an order of magnitude higher than the frequencies of the naturally shed vortices using meridional arrays of synthetic jets that issue normal to the surface. In addition to harmonic high-frequency control, the effects of amplitude-modulated actuation are also investigated with the objective of imposed organization of the separating shear layer at low frequencies.

It is shown that high-frequency control has a significant effect on the structure of the separated flow domain over the entire range of Reynolds numbers. In particular, at the low end of the range, the extent of the recirculating domain in the central plane is vastly diminished, the vorticity becomes concentrated near the juncture between the hemisphere and the flat surface, and the separation line is displaced more than 20 deg. These effects are also prevalent at the higher Reynolds numbers and the effectiveness of the actuation is only limited by the available momentum coefficient of the jets. It is also shown that the streamwise location of the actuators (with respect to the separation) cannot only delay separation, but also move it upstream. Given the three-dimensional separation line (streamwise horseshoe shaped), the present work has also shown that for any crossflow and momentum coefficient there is an optimal actuation location for the maximum delay of separation and minimal recirculating flow domain. Alternatively, the performance can be optimized by adjusting the momentum coefficient at a given position.

The actuation leads to a substantial reduction in the magnitude of the estimated turbulent kinetic energy within the recirculating flow domain. Spectral analysis shows that the reduction of energy occurs over all flow scales and the suppression is particularly effective on large-scale motions. The reduction in turbulent kinetic energy also suggests a reduction in turbulent energy production. In addition to pure high-frequency control, amplitude-modulated actuation of the high-frequency waveform is used to enhance organized, phase-coherent large-scale motions over the flow-receptive low frequencies. In the presence of amplitude-modulated actuation, the flow contains spectral components at the modulating frequency (typically an order of magnitude lower than the high carrier frequency) and its higher harmonics, in addition to the high (carrier) frequency. This actuation approach still lowers the energy across the scales with the exception of the motions at the modulation frequency. However, in contrast to the harmonic high-frequency actuation, the modulated control does not significantly alter the domain of the separated flow, but it seems to more evenly distribute the two-component turbulent kinetic energy and also lowers its overall magnitude. It is believed that the amplitude-modulated, high-frequency control approach is a good candidate when correction of optical aberrations is sought to be achieved by the adaptive optics approach. Finally, an important component of the present work was a demonstration of improved spanwise control authority. Because the separation line is horseshoe shaped, the effectiveness of the actuator array is limited by the varying streamwise distance between individual actuators and the separation line. Therefore, a case is presented in the current work where the flow is forced to separate along a spanwise line upstream of the actuators such that the lateral uniformity of the actuation effectiveness is improved.

Acknowledgment

This research was supported by the U.S. Air Force Research Laboratory, Air Vehicle Directorate, Wright–Patterson Air Force Base, Ohio.

References

[1] Jumper, E. J., and Fitzgerald, E. J., "Recent Advances in Aero-Optics," *Progress in Aerospace Sciences*, Vol. 37, No. 3, 2001, pp. 299–339. doi:10.1016/S0376-0421(01)00008-2

[2] Smith, D. R., Amitay, M., Kibens, V., Parekh, D., and Glezer, A., "Modification of Lifting Body Aerodynamics Using Synthetic Jet Actuators," AIAA Paper 1998-0209, Jan. 1998.

[3] Amitay, M., and Glezer, A., "Role of Actuation Frequency in Controlled Flow Reattachment Over a Stalled Airfoil," *AIAA Journal*, Vol. 40, No. 2, 2002, pp. 209–216. doi:10.2514/2.1662

[4] Choi, H., Jeon, W.-P., and Kim, J., "Control of Flow Over a Bluff Body," *Annual Review of Fluid Mechanics*, Vol. 40, No. 1, 2008, pp. 113–139. doi:10.1146/annurev.fluid.39.050905.110149

[5] de Jonckheere, R., Russell, J. J., and Chou, D. C., "High Subsonic Flowfield Measurements and Turbulent Flow Analysis Around a Turret Proturberance," AIAA Paper 82-0057, Jan. 1982.

[6] Purohit, S. C., Shang, J. S., and Hankey, W. L., "Effect of Suction on the Wake Structure of a Three-Dimensional Turret," AIAA Paper 83-1738, July 1983.

[7] Snyder, C. H., Franke, M. E., and Masquelier, M. L., "Wind-Tunnel Tests of an Aircraft Turret Model," *Journal of Aircraft*, Vol. 37, No. 3, 2000, pp. 368–376. doi:10.2514/2.2625

[8] Gordeyev, S., Jumper, E. J., Ng, T. T., and Cain, A. B., "The Optical Environment of a Cylindrical Turret with a Flat Window and the Impact of Passive Control Devices," AIAA Paper 2005-4657, June 2005.

[9] Gordeyev, S., Post, M. L., McLaughlin, T., Ceniceros, J., and Jumper, E. J., "Aero-Optical Environment Around a Conformal-Window Turret," *AIAA Journal*, Vol. 45, No. 7, 2007, pp. 1514–1524. doi:10.2514/1.26380

[10] Vukasinovic, B., and Glezer, A., "Control of a Separating Flow Over a Turret," AIAA Paper 2007-4506, June 2007.

[11] Toy, N., Moss, W. D., and Savory, E., "Wind Tunnel Studies on a Dome in Turbulent Boundary Layers," *Journal of Wind Engineering and Industrial Aerodynamics*, Vol. 11, Nos. 1–3, 1983, pp. 201–212. doi:10.1016/0167-6105(83)90100-9

[12] Vukasinovic, B., Glezer, A., Gordeyev, S., Jumper, E., and Kibens, V., "Active Control and Optical Diagnostics of the Flow over a Hemispherical Turret," AIAA Paper 2008-598, Jan. 2008.

[13] Hunt, J. C. R., Abell, C. J., Peterka, J. A., and Woo, H., "Kinematical Studies of the Flows Around Free or Surface-Mounted Obstacles: Applying Topology to Flow Visualization," *Journal of Fluid Mechanics*, Vol. 86, No. 1, 1978, pp. 179–200. doi:10.1017/S0022112078001068

[14] Ayoub, A., and Karamcheti, K., "An Experiment on the Flow Past a Finite Circular Cylinder at High Subcritical and Supercritical Reynolds Numbers," *Journal of Fluid Mechanics*, Vol. 118, No. 1, 1982, pp. 1–26. doi:10.1017/S0022112082000937

[15] Adrian, R. J., "Particle-Imaging Techniques for Experimental Fluid Mechanics," *Annual Review of Fluid Mechanics*, Vol. 23, No. 1, 1991, pp. 261–304. doi:10.1146/annurev.fl.23.010191.001401

[16] Westerweel, J., "Theoretical Analysis of the Measurement Precision in Particle Image Velocimetry," *Experiments in Fluids*, Vol. 29, No. 7, 2000, pp. S003–S012. doi:10.1007/s003480070002

[17] Comte-Bellot, G., "Hot-Wire Anemometry," *Annual Review of Fluid Mechanics*, Vol. 8, 1976, pp. 209–231. doi:10.1146/annurev.fl.08.010176.001233

[18] Achenbach, E., "Experiments on the Flow Past Spheres at Very High Reynolds Numbers," *Journal of Fluid Mechanics*, Vol. 54, 1972, pp. 565–575. doi:10.1017/S0022112072000874

[19] Taneda, S., "Visual Observations of the Flow Past a Sphere at Reynolds Numbers Between 10^4 and 10^6," *Journal of Fluid Mechanics*, Vol. 85, No. 1, 1978, pp. 187–192. doi:10.1017/S0022112078000580

[20] Achenbach, E., "Distribution of Local Pressure and Skin Friction Around a Circular Cylinder in Cross-Flow up to $Re = 5 \times 10^6$," *Journal of Fluid Mechanics*, Vol. 34, No. 4, 1968, pp. 625–639. doi:10.1017/S0022112068002120

[21] Vukasinovic, B., Glezer, A., and Rusak, Z., "Experimental and Numerical Investigation of Controlled, Small-Scale Motions in a Turbulent Shear Layer," *Proceedings of the 3rd International Symposium of Integrating CFD and Experiments in Aerodynamics*, U.S. Air Force Academy, Colorado Springs, CO, June 2007.

[22] Zubair, F. R., Freeman, A. P., Piatrovich, S., Shockro, J., Ibrahim, Y. N., and Catrakis, H. J., "Large Scale Turbulence Suppression Control for Direct Reduction of Aero-Optical Aberrations," AIAA Paper 2007-4008, June 2007.

[23] Visbal, M. R., and Rizzetta, D. P., "Effect of Flow Excitation on Aero-Optical Aberration," AIAA Paper 2008-1074, Jan. 2008.

[24] Kim, H. J., and Durbin, P. A., "Observation of the Frequencies in a Sphere Wake and of Drag Increase by Acoustic Excitation," *Physics of Fluids*, Vol. 31, No. 11, 1988, pp. 3260–3265. doi:10.1063/1.866937

[25] Wiltse, J. M., and Glezer, A., "Manipulation of Free Shear Flows Using Piezoelectric Actuators," *Journal of Fluid Mechanics*, Vol. 249, No. 1, 1993, pp. 261–285. doi:10.1017/S002211209300117X

[26] Vukasinovic, B., and Glezer, A., "Transitory Fluidic Control of Turbulent Shear Flows," AIAA Paper 2006-3227, June 2006.

N. Chokani
Associate Editor